UC Davis

UC Davis Previously Published Works

Title

Role of Copper Doping in Modulating the Thermoelectric Properties of Eu11Zn4Sn2As12

Permalink

https://escholarship.org/uc/item/3wj8058q

Journal

ACS Applied Energy Materials, 9(11)

ISSN

2574-0962

Authors

Miramontes Ruiz, C

Wróblewska, M

Toberer, ES

et al.

Publication Date

2026-06-08

DOI

10.1021/acsaem.6c00664

Copyright Information

This work is made available under the terms of a Creative Commons Attribution License, available at https://creativecommons.org/licenses/by/4.0/

Peer reviewed

eScholarship.org Powered by the California Digital Library
University of California

Role of Copper Doping in Modulating the Thermoelectric Properties of $Eu_{11}Zn_4Sn_2As_{12}$

Christopher Miramontes Ruiz,[1] Maria Wróblewska,[2] Eric S. Toberer,[2] and Susan M. Kauzlarich[1*]

[1]Department of Chemistry, One Shields Ave, University of California, Davis, California 95616, United States

[2] Department of Physics, Colorado School of Mines, Golden, Colorado 80401, United States

* Corresponding Author: Susan M. Kauzlarich, smkauzlarich@ucdavis.edu

Abstract

Layered Zintl phase materials are of great interest due to their directional bonding and electronic properties. $Eu_{11}Zn_4Sn_2As_{12}$ is a p-type semiconductor that has been proposed to undergo 3D-to-2D electronic transport as the carrier concentration increases. This commensurately modulated structure in space group $R\bar{3}m$ has been shown to improve its thermoelectric properties upon Na doping, concurrently decreasing electrical resistivity while maintaining a large Seebeck coefficient. In this study, $Eu_{11}Zn_4Sn_2As_{12}$ was doped with Cu with the goal of substituting in the $[Zn_2As_3]^{5-}$ defect hexagonal layers to improve electrical transport. Resistivity decreased from ~5900 mΩ cm to ~30 mΩ cm as the carrier concentration increased, and degenerate semiconductor behavior was observed in some doped samples. A maximum zT_{600K} of 0.24 for x = 0.6 was reached.

Keywords: Thermoelectrics, thermal conductivity, resistivity, carrier concentration, layered structure

Introduction

Thermoelectric materials have garnered significant interest in recent years as a source of renewable energy due to their ability to convert waste heat into electricity.[1,2] Some of these materials have also been investigated for other applications, such as photovoltaic-thermoelectric hybrid systems[3] and as platforms for quantum phenomena.[4] While thermoelectric materials span a broad field of compounds, one subsection that has shown promise is Zintl phases. Zintl phases are a subset of intermetallic compounds composed of ionic bonding, in which the electropositive atoms donate their electrons to the more electronegative atoms, and covalent bonding in the form of clusters or layered phases.[5] This combination of bonding gives rise, in many cases, to semiconducting properties. Layered Zintl phases exhibit anisotropy and tunability of the anion motifs and at cation sites via doping or substitution.[6, 7] In

order to understand how well a thermoelectric material can behave, it is important to consider the dimensionless figure of merit, zT.[8] This thermoelectric figure of merit is given by the following equation: $zT = \frac{S^2T}{\rho\kappa}$ where S is the Seebeck coefficient, ρ is the electrical resistivity, κ is the thermal conductivity, and T is the absolute temperature. The challenge of obtaining a high figure of merit comes from the interdependence of S, ρ, and κ. In a single parabolic band model, the Seebeck coefficient and carrier concentration are inversely related.[9]

The complex layered Zintl compound $Eu_{11}Zn_4Sn_2As_{12}$ has recently been investigated for its thermoelectric properties.[10,11] The structure of $Eu_{11}Zn_4Sn_2As_{12}$, shown in Figure 1, consists of layers of Eu^{2+} cations separating $[Zn_2As_3]^{5-}$ hexagonal layers and $[Sn_2As_6]^{12-}$ ethane-like structures. The structure is valence precise as shown by $11Eu^{2+} + 2[Zn_2As_3]^{5-} + [Sn_2As_6]^{12-}$.[10] The $[Zn_2As_3]^{5-}$ hexagonal layer is also shown in Figure 1 and can be described as a defect hexagonal layer, with half of the Zn sites vacant in random order throughout the structure. Similar defect hexagonal layers have been observed in various compounds, including Eu_2ZnSb_2,[12] Sr_2ZnSb_2,[13] $Eu_{3-\delta}Zn_xSn_yAs_3$,[14] and BaAgAs.[15] $Eu_{11}Zn_4Sn_2As_{12}$ was initially discovered as single crystals from a flux reaction, and quantum chemical calculations showed that the defect hexagonal sheets are best described by delocalized bonding.[10] In light of the complex unit cell and heavy constituent elements, low thermal conductivity was predicted, and polycrystalline samples of Na-doped $Eu_{11}Zn_4Sn_2As_{12}$ were synthesized to investigate the thermoelectric properties.[11] The interplay between its low thermal conductivity, moderate carrier concentration, and potential magnetic interactions makes this compound an intriguing addition to the broader class of layered Zintl thermoelectrics.

Layered materials have been shown to possess 2D electronic structures that can arise from 3D structures.[16,17] From density functional theory (DFT) calculations, the Fermi surface of $Eu_{11}Zn_4Sn_2As_{12}$ was found to transition from 3D to 2D electronic structure with increasing carrier concentration, providing justification for investigating its thermoelectric properties.[11] Upon the addition of Na as a dopant, the semiconductor's resistivity decreased nearly 5-fold. Although the resistivity dropped dramatically, it still exceeds that of competing layered materials. The optimal carrier concentration required to transition to a 2D electronic structure, as suggested by theoretical calculations, is 10^{19} h^+ cm^{-3},[11] but this value was not achieved with cation doping due to the solubility limit of Na within this phase. It was suggested that doping at the Zn cation sites within the defect hexagonal layer may provide a route towards increasing the carrier concentration.[11]

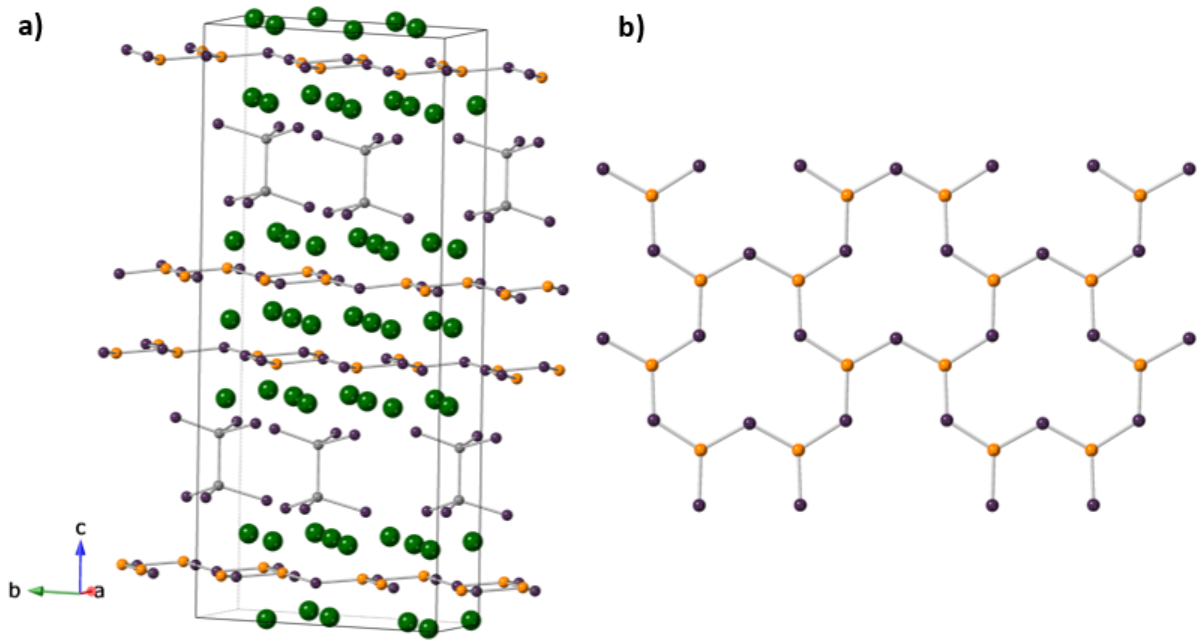


Figure 1. a) A view of the layered structure of $Eu_{11}Zn_4Sn_2As_{12}$ showing Eu atoms, $[Zn_2As_3]^{5-}$ defect hexagonal sheets, and $[Sn_2As_6]^{12-}$ ethane-like structures. b) Top view along the *c*-axis of the defect hexagonal sheets (while this view shows an ordered defect structure, the vacant Zn sites are random in the hexagonal sheet). Eu atoms are depicted in green, Zn in orange, Sn in gray, and As in dark purple.

This work focuses on the $[Zn_2As_3]^{5-}$ defect hexagonal sheets within $Eu_{11}Zn_4Sn_2As_{12}$ by investigating the impact of Cu^+ substitution on the Zn^{2+} sites. Cu has been shown to improve the thermoelectric properties in Zintl and other phases.[5,18–20] Recently, Cu has been substituted for Zn in ZnSb and showed dramatic improvement of the transport properties, resulting in a thermoelectric efficiency of 1 at 600 K.[19] Cu^+ is expected to substitute for Zn^{2+} because of the similarity in size and electronegativity, while also increasing the number of holes in the $[Zn_2As_3]^{5-}$ defect hexagonal sheets. It is also possible that Cu^+ could fill vacancy sites within the defect hexagonal sheet, but in either case, the addition of Cu should increase the carrier concentration without greatly perturbing the structure. $Eu_{11}Zn_4Sn_2As_{12}$ has very low thermal conductivity,[11] below 1 W/m K, and substituting Cu^+ for Zn^{2+} may further reduce the lattice thermal conductivity through point defect scattering.[21] The Seebeck coefficient remained high for the previously reported effort on Na^+ doping,[11] so further investigation to increase the carrier concentration is warranted.

Experimental

Synthesis

The EuAs binary phase was prepared from stoichiometric amounts of Eu metal (Stanford Materials, 99.99%) and As lump (Luciteria, 99.999%). The elements were weighed in an Ar-filled glovebox and added to a stainless-steel ball mill vial containing two stainless-steel balls, then sealed in a Mylar bag. The vial was placed in a SPEX 8000M mixer mill and milled for 30 min. The vial was transferred back to the glovebox and scraped with a stainless-steel chisel. It was then resealed and milled for an additional 30 min to homogenize. The ball mill was scraped, and the resulting powder was added to a Ta tube (OD 0.375 x 0.02) that had been sealed on one end in an Ar(g) arc welder. The Ta tube was crimped at the top, transferred to the arc welder, and sealed under Ar(g). Once the Ta tube was sealed, it was placed in a fused silica tube under vacuum and sealed. The reaction vessel was heated in a box furnace to 850 °C at a rate of 200 °C/h, annealed for 24 h. The furnace was turned off, and the sample was allowed to cool to room temperature. The reaction vessel was transferred to a glovebox, and the product was ground and sieved for powder X-ray diffraction measurements. Powder X-ray diffraction and Rietveld refinement are shown in the Supporting Information (SI) Figure S1 and Table S1.

$Eu_{11}Zn_{4-x}Cu_xSn_2As_{12}$ samples were made by combining EuAs, prepared as described above, with stoichiometric amounts of the elements to prepare 3 g of product: Zn flake (Assay, 99.98%), Sn shot (Alfa Aesar,99.8%), Cu shot (Furuchi Chem, 99.999%), and As lumps. In an Ar-filled glovebox, the elements and EuAs(s) powder were placed in a stainless-steel ball mill with two stainless-steel balls and sealed in a mylar bag. The vial was milled using the same procedure described above, and the resulting powder (3 g) was transferred into a Ta tube and sealed as described above. The reaction vessels were heated to 800 °C at a rate of 200 °C, annealed for 96 h, and then furnace cooled to room temperature. The reaction vessel was transferred to a glovebox, and the product was ground and sieved for powder X-ray diffraction measurements.

Spark Plasma Sintering (SPS)

The resulting samples were ground to a fine powder using a mortar and pestle and then sieved. They were loaded into a 12.7 mm graphite die with graphite foil on either end. The graphite die was loaded into the Dr. Sinter Junior Spark Plasma Sintering system (Fuji Electronic Industrial Co., LTD) under an Ar(g) atmosphere. The sample was heated to 545 ºC in eight minutes, then to 645 ºC, where it was held for ten minutes. The force was increased from 6 kN to 10.2 kN at 500 ºC. After the allotted time of 10 min, the graphite die was cooled to room temperature and yielded pellets that were ≥ 95% from the theoretical density, determined by the Archimedes' method.

Powder X-Ray Diffraction (PXRD)

Samples were analyzed before and after SPS. All samples appeared to be air-stable and were plated and handled under ambient conditions. A small piece of the sintered sample pellet was ground in a mortar and pestle for PXRD analysis. Samples were plated onto a zero-background X-ray quartz plate, and diffraction was performed with a Bruker D8 Advance Eco diffractometer with Cu Kα radiation (λ = 1.5405 Å) at 40 kV and 25 mA at room temperature. Data was collected with a 0.01 step size and a 2θ range from 20° - 80°. The TOPAS5 software package was used for Rietveld refinement,[11] and the refinement models were generated from the EuAs and $Eu_{11}Zn_4Sn_2As_{12}$ crystallographic information files (CIFs).[22,23] No preferred orientation is evident from PXRD of either as-prepared powder or a pressed pellet.

Scanning Electron Microscopy (SEM) and Energy-Dispersive-X-Ray Spectroscopy (EDS)

A piece of sintered pellet was encased in an epoxy puck and polished using both sandpaper and a polishing wheel (1 µm colloidal diamond suspension) for SEM/EDS analysis on the FEI Scios DualBeam FIB/SEM equipped with an Oxford X-Max 50 mm^2 Si drift detector. Secondary electron images were collected at an accelerating voltage of 20 kV with a 1.6 nA beam current containing an Everhart-Thornley detector.

Thermal Conductivity

A Netzsch Laser Flash Analysis (LFA) 475 Microflash instrument was used to measure the thermal diffusivity of the pellets (polished flat and parallel and sprayed with graphite to ensure laser absorption). Thermal conductivity was calculated using thermal diffusivity using the equation κ = λδCp, where κ is thermal conductivity, λ is thermal diffusivity, δ is the sample density, and Cp is the Dulong-Petit heat capacity. The C_p for x = 0.4 and x = 0.6 was calculated using the rule of mixtures, where C_p (total) = (C_p $Eu_{11}Zn_{4-x}Cu_xSn_2As_{12}$ * mass % $Eu_{11}Zn_{4-x}Cu_xSn_2As_{12}$) + ($C_p$ $Eu_5Sn_2As_6$ * mass % $Eu_5Sn_2As_6$).[24] The mass percents were obtained from Rietveld refinement and used to calculate the thermal conductivity for those specific samples.

Seebeck, Resistivity, and Hall Measurement

Seebeck coefficient measurements were obtained from a custom-built instrument under nitrogen atmosphere and pressure of 300 Torr from 300 to 600K.[25] Resistivity and Hall measurements were obtained with an in-house-built instrument using the van der Pauw geometry. Hall coefficient measurements used 80 mA current and 1 T magnetic field.[26]

Results and Discussion

Samples of $Eu_{11}Zn_{4-x}Cu_xSn_2As_{12}$ were prepared by mechanically alloying the powders of EuAs, Zn, Cu, Sn, and As in stoichiometric ratios and heat treating the powder in a Ta tube at 800 °C

for 96 h. Powder X-ray diffraction (PXRD) patterns were collected on the as-synthesized powders and on pieces of the pressed pellets that were ground and sieved. $Eu_{11}Zn_{4-x}Cu_xSn_2As_{12}$ was stable to air, and the diffraction patterns were collected under ambient conditions. PXRD patterns of $Eu_{11}Zn_{4-x}Cu_xSn_2As_{12}$ (x = 0, 0.2, 0.4, 0.6) are shown in the range from 20° to 50° in Figure 2, with complete Rietveld refinements of the data from 20° to 80° provided in SI, Figure S2-S3. A pressed pellet PXRD is shown in SI, Figure S4, to demonstrate that a pressed pellet shows no preferred orientation, with reflection intensities similar to those observed from the powdered samples shown in Figure 2. The patterns show that x = 0 and x = 0.2 are phase pure, whereas x = 0.4 and x = 0.6 both exhibit additional small peaks that match those of $Eu_5Sn_2As_6$. Lattice parameters and weight percentages of minor impurities in the final product for the samples of $Eu_{11}Zn_{4-x}Cu_xSn_2As_{12}$ (x = 0,0.2, 0.4, 0.6) were obtained from Rietveld refinements and provided in Table 1.

The *a*-axis decreases slightly, while the *c*-axis increases with increasing Cu content, up to x = 0.6; this suggests that Cu^+ is being incorporated into either a Zn^{2+} site or a vacant site within the hexagonal layer.[27] Either substitution should reduce the *a*-axis while increasing the *c*-axis, because Cu^+ ions are slightly smaller than Zn^{2+} ions and carry a smaller charge. The presence of $Eu_5Sn_2As_6$ in the product may indicate that above x = 0.4, the structure cannot compensate for the Cu doping, suggesting a solubility limit and leading to the formation of the $Eu_5Sn_2As_6$ phase.[28] The weight percent of $Eu_5Sn_2As_6$ was about 3% for x = 0.4 and 0.6. However, the changes in the lattice parameters for x = 0.6 suggest that no additional Cu is incorporated, as both the *a* and *c* axes become smaller for this composition. This is more clearly shown in plots of lattice parameters, Figure 3. If we compare these compounds with the Na-doped samples of

$Eu_{11-x}Na_xZn_4Sn_2As_{12}$, x_{max} = 0.075, whereas $Eu_{11}Zn_{4-x}Cu_xSn_2As_{12}$ is doped at a much higher concentration, x_{max} = 0.4.

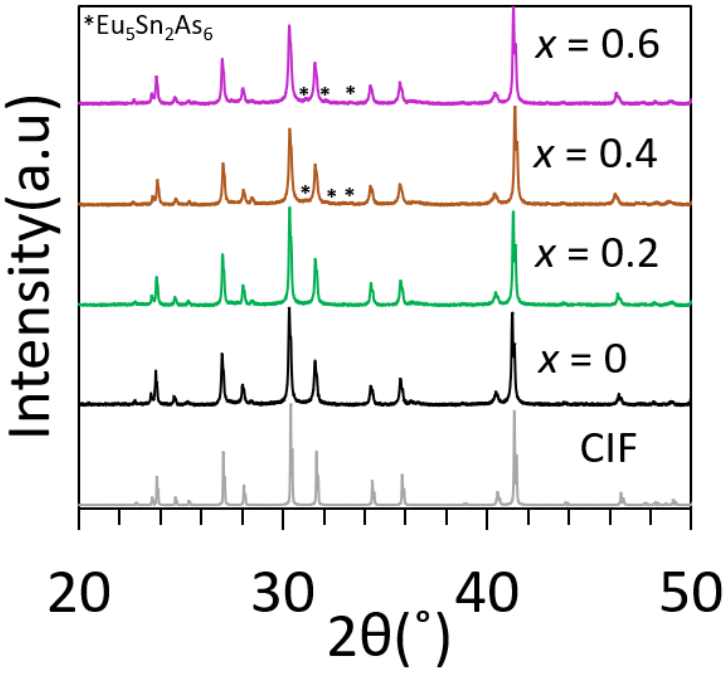


Figure 2. Stacked plot of a portion of the PXRD patterns of $Eu_{11}Zn_{4-x}Cu_xSn_2As_{12}$ (x = 0, 0.2, 0.4, 0.6) compared with the calculated pattern of $Eu_{11}Zn_4Sn_2As_{12}$, with * indicating peaks consistent with $Eu_5Sn_2As_6$.

Table 1. Rietveld Refinement Statistics for $Eu_{11}Zn_{4-x}Cu_xSn_2As_{12}$ (x = 0, 0.2, 0.4, 0.6)

x	**$Eu_{11}Zn_{4-x}Cu_xSn_2As_{12}$ wt %**	**$Eu_5Sn_2As_6$ wt %**	**Unit Cell Parameters *a*(Å) *c*(Å) *V*(Å³)**	**Gof(%) Rp(%) Rwp(%)**
0	100	-	4.3771(5) 46.896(1) 778.13(2)	1.68 11.20 13.83
0.2	100	-	4.3746(1) 46.961(1) 778.31(5)	1.73 11.32 13.97
0.4	97.8(9)	2.17(5)	4.3663(4) 47.093(8) 777.55(6)	1.83 9.48 12.59
0.6	97.1(8)	2.84(2)	4.3709(2) 47.000(2) 777.65(7)	1.74 10.67 13.33

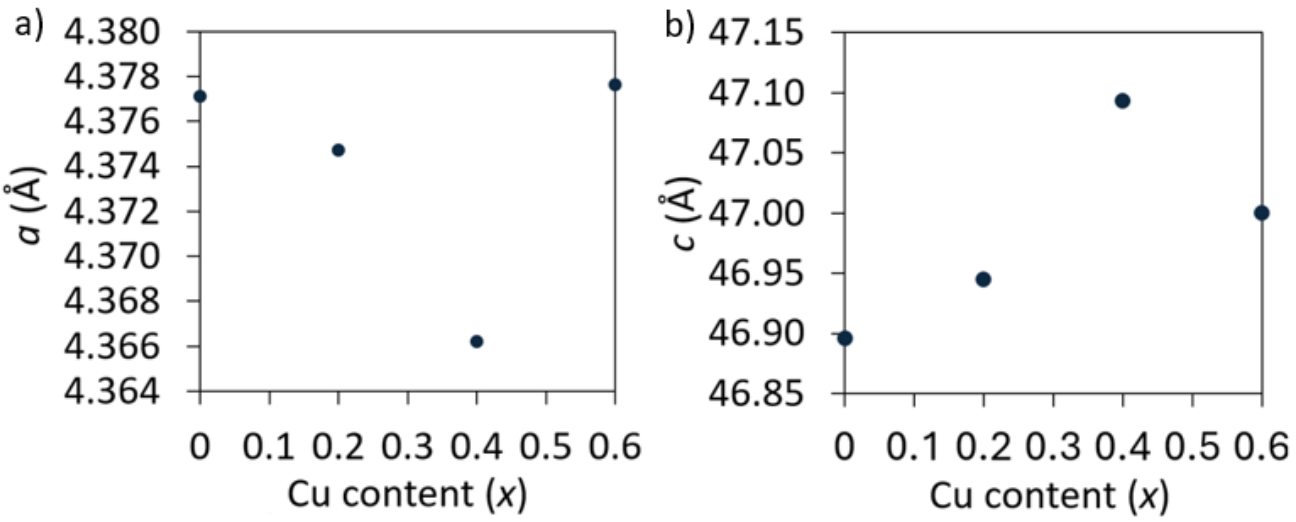


Figure 3. Lattice parameters as a function of Cu content, *x,* for a) the *a*-axis and b) the *c*-axis.

Figure 4 shows a secondary electron image and EDS elemental maps of $Eu_{11}Zn_{4-x}Cu_xSn_2As_{12}$ with the Cu content (x = 0.4). The secondary electron image shows no obvious secondary phase. The elemental maps show a homogeneous distribution of all elements of interest. The composition determined from EDS for x = 0.4 is $Eu_{10.52}Zn_{3.20}Cu_{0.40}Sn_{2.04}As_{12.8}$, consistent with the amount of Cu added. SEM micrographs and EDS elemental maps for x = 0, 0.2, and 0.6 are provided in the SI, Figures S5-S7, along with a Table of compositions determined from EDS (SI, Table S2).

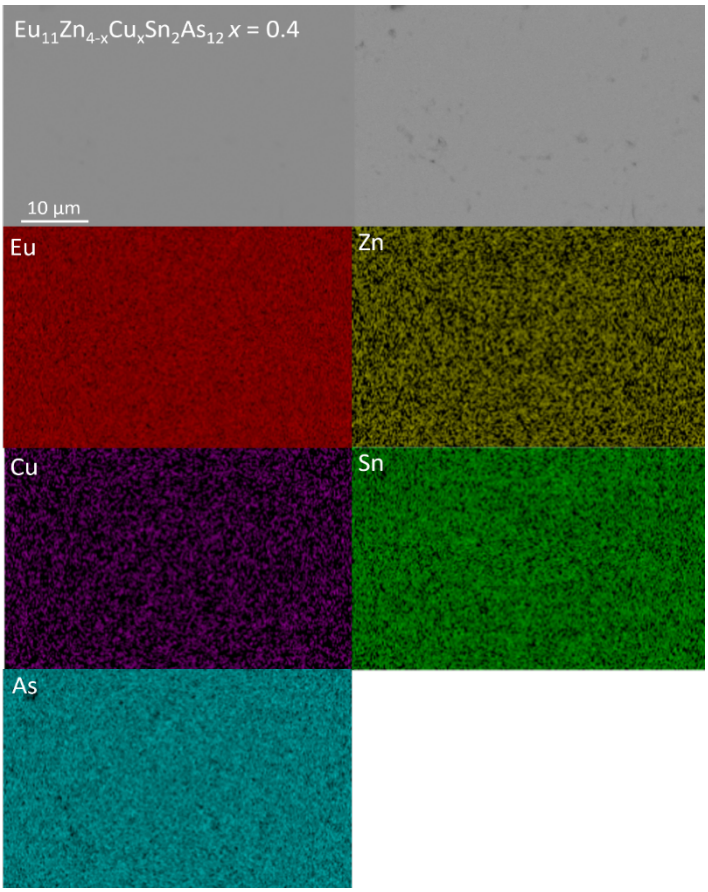


Figure 4. The secondary electron (SE) image, backscattering electron image (BSE) and the elemental maps for Eu, As, Sn, Zn, and Cu are homogeneously dispersed in the pressed pellet for x = 0.4. The scale bar indicated in the SE image applies to all the elemental maps.

The temperature-dependent total thermal conductivity and lattice thermal conductivity of $Eu_{11}Zn_{4-x}Cu_xSn_2As_{12}$ (x = 0, 0.2, 0.4, 0.6) are shown in Figure 5. The electronic thermal conductivity (κ_e) was estimated using the Wiedemann-Franz relation $\kappa_e = L\sigma T$, where L is the Lorenz number, which is calculated from the Seebeck coefficient according to the equation, $L = 1.5 + \exp\left(-\frac{|S|}{116}\right)$.[29] The lattice thermal conductivity (κ_L) was calculated by subtracting the electronic thermal conductivity from the total thermal conductivity (shown in Figure 5a). The lattice thermal conductivity for x = 0 is the same as previously reported for $Eu_{11}Zn_4Sn_2As_{12}$.[11] There is a slight increase in total thermal conductivity with increasing Cu substitution for Zn, but

the value of the total thermal conductivity remains lower than that of the previously published Na-doped samples.[11] The values of the total thermal conductivity range from 0.65 to 0.5 W/m K, and these low values are lower or on par with other layered phases, such as $Eu_5Sn_2As_6$[28] and Eu_2ZnSb_2,[12] as well as other complex Zintl phases, such as the $Yb_{14-x}Ce_xMnSb_{11}$.[30] Comparing the lattice thermal conductivities of the samples in Figure 5b, it is evident that heat transport is dominated by κ_L. It was proposed that diffusons may contribute to the low lattice thermal conductivity of this compound.[11] Diffusons play a role in the high-temperature regime, so here it is most likely that phonon-phonon scattering dominates heat transport. The lattice thermal conductivity is about the same for $x = 0$ and $x = 0.2$. While these values of x increase the carrier concentration beyond the maximum Na content of $x \sim 0.08$,[11] it is likely that the single parabolic band (SPB) model for calculating κ_e is valid for these compositions. The band structure of $Eu_{11}Zn_4Sn_2As_{12}$ has been previously published and a cartoon is provided in Figure 6.[10,11] With increasing x in $Eu_{11}Zn_{4-x}Cu_xSn_2As_{12}$, there should be an increase in hole carriers and a transition to a degenerate multi-band. Therefore, the slight increase in κ_L with Cu concentration may be attributed to either the small amount of the secondary phase, $Eu_5Sn_2As_6$, or a transition from a SPB to a degenerate or multivalley band(s). $Eu_5Sn_2As_6$ thermoelectric properties have been investigated, and it shows higher thermal conductivity than $Eu_{11}Zn_4Sn_2As_{11}$, with a room temperature value of (~1.2 W/m K at 300 K).[28] Based on the calculated band structure and supported by the weighted mobility plot shown in the SI, Figure S8, the $x = 0.4$, 0.6 samples are not consistent with a single parabolic band model and exhibit different characteristics compared to $x = 0.2$ and the Na-doped compounds.[11] The Lorenz number calculated from the equation above is approximated for a SPB model, but that is not the case for $x = 0.4$, 0.6.[29] Given the appearance of multiband transport in the weighted mobility, the calculated κ_e is likely not adequate for the $x = 0.4$, 0.6 samples. However, regardless of the calculated κ_e, the lattice thermal conductivities are comparable, and the total low lattice thermal conductivity is comparable to other arsenide structures, such as $Eu_{14}ZnAs_{11}$,[31] $Eu_{11}CdAs_{11}$,[31] and $Eu_{21}Zn_4As_{18}$.[32]

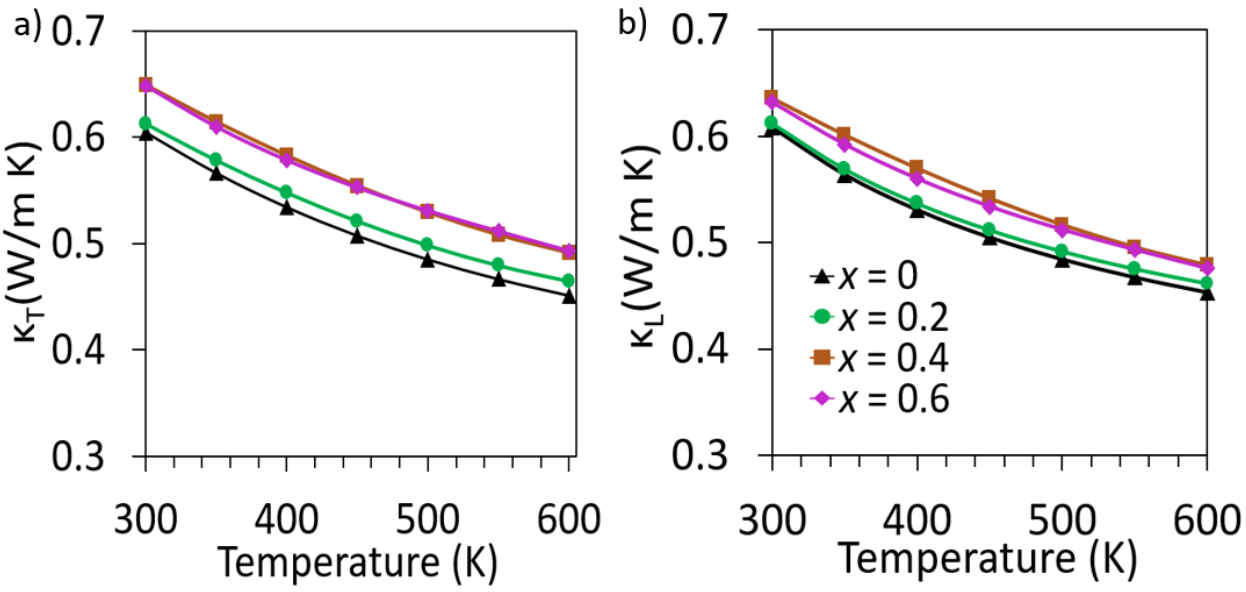


Figure 5. a) Total thermal conductivity and b) lattice thermal conductivity from 300 to 600 K of $Eu_{11}Zn_{4-x}Cu_xSn_2As_{12}$ (x = 0, 0.2, 0.4, 0.6).

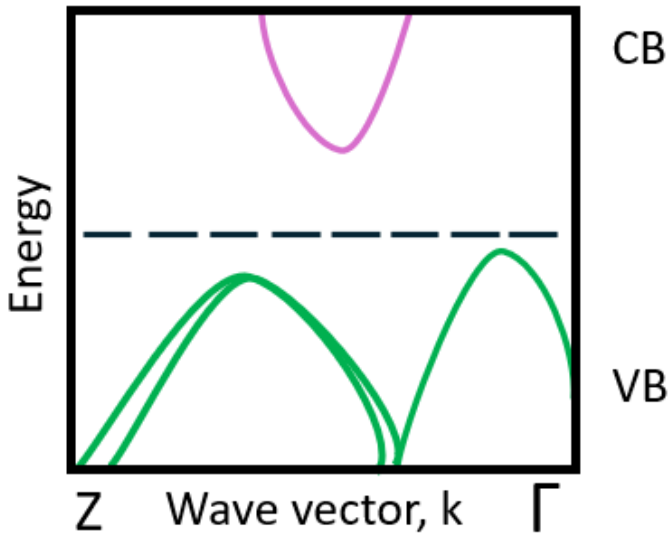


Figure 6. Cartoon depiction of a portion of the band structure of $Eu_{11}Zn_4Sn_2As_{12}$from Γ to Z, showing the indirect band gap and two different bands along the valence band.

The Hall mobility and carrier concentration of $Eu_{11}Zn_{4-x}Cu_xSn_2As_{12}$ (x = 0, 0.2, 0.4, and 0.6) are shown in Figure 7. For x = 0, the carrier concentration is 10^{17} h^+ cm^{-3}, and the maximally doped samples (x = 0.4, 0.6) increase to ~ 10^{19} h^+ cm^{-3}, consistent with Cu^{1+} doping. The Hall carrier

concentration shows a 10-fold increase compared to previous studies of Na doping, and the initial low carrier concentration of $Eu_{11}Zn_4Sn_2As_{12}$ is consistent with published data.[11] The optimal carrier concentration for many thermoelectric materials falls between 10^{19} and 10^{20}, which this material almost reaches but falls short. A plot comparing the highest Na-doped sample to the Cu-doped samples is available in the SI, Figure S9. Hall mobility increases almost twofold from ~ 13 cm^2/Vs to ~ 23 cm^2/Vs over the range x = 0 - 0.6 and decreases with increasing temperature due to charge-carrier scattering from phonons. Mobility and weighted mobility also increase for the Na-doped compound. This was interpreted as possible grain boundary scattering, which may also be present in the x = 0.4 and 0.6 compositions.[11] In this example, Cu is likely to be incorporated into the hexagonal net, thereby reducing the scattering effect as seen in $Mg_3Sb_{1.5}Bi_{0.5}$ and $Bi_{0.5}Sb_{1.5}Te_3$.[27,33] Since Cu may not have a preferred site, vacancies within the hexagonal layer can also serve as sites for Cu to fill, thereby enhancing mobility.

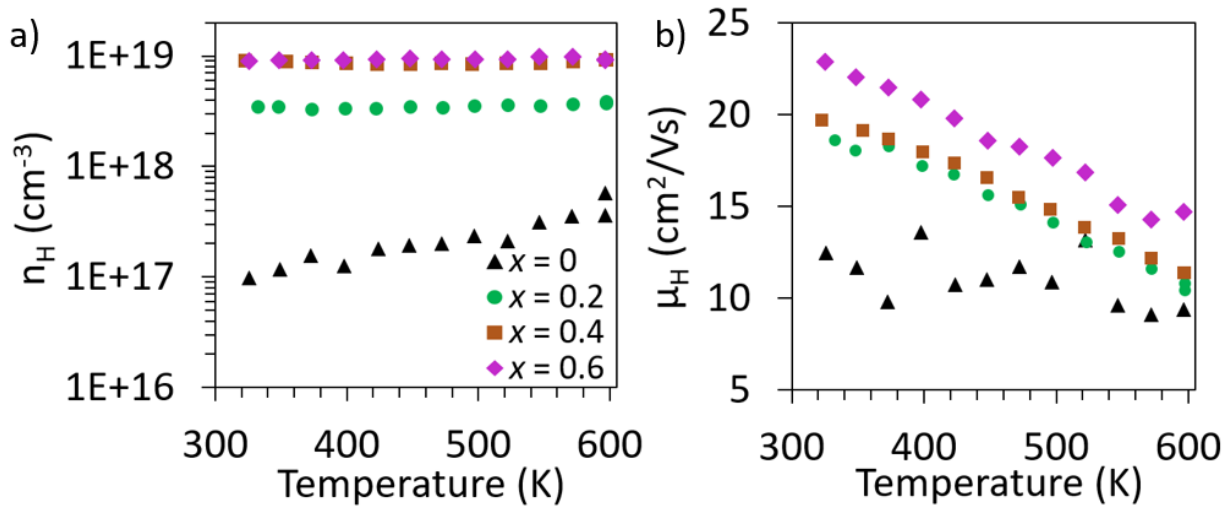


Figure 7. a) Carrier concentration and b) Hall mobility for $Eu_{11}Zn_{4-x}Cu_xSn_2As_{12}$ (x = 0, 0.2, 0.4, 0.6) from 300 to 600 K.

The resistivity and Seebeck coefficients of $Eu_{11}Zn_{4-x}Cu_xSn_2As_{12}$ (x = 0, 0.2, 0.4, and 0.6) were measured from 300 to 600 K and are shown in Figure 8. The resistivity decreases significantly compared to the pristine sample. From previous theoretical calculations,[11] the pristine compound was predicted to have a resistivity of 4000 mΩ cm at 10^{17} cm^{-3}, which is similar to the experimental data shown here. The room temperature resistivity for x = 0 is ~5900 mΩ cm, and it decreases to ~ 30 mΩ cm for the x = 0.6 sample. This indicates the effectiveness of Cu doping into the Zn sites. At sample x = 0.6, resistivity remains close to that of x = 0.4, which may be indicative of a solubility limit. The resistivity increases with temperature for the x = 0.2-0.6 samples, consistent with that of a degenerate semiconductor, as observed in other materials.[34–

[36] Although samples x = 0.4 and x = 0.6 both contain the $Eu_5Sn_2As_6$ impurity, this impurity should increase resistivity, as $Eu_5Sn_2As_6$ has a high resistivity of 462 mΩ cm at room temperature.[28] The Seebeck values for all samples are positive, indicating that the samples are p-type semiconductors. The S values for all samples increase with temperature, and for the pristine sample, the values are high, around ~500 to ~600 μV/K, consistent with previous results.[11] As the doping amount of Cu in $Eu_{11}Zn_{4-x}Cu_xSn_2As_{12}$ increases, the Seebeck coefficient decreases, consistent with an impact of carrier concentration on the Seebeck coefficient.[37] This behavior differs from that observed in the Na-doped structure, where the Seebeck coefficient remains high even as resistivity decreases. The reason these properties were decoupled is attributed to the anisotropic Fermi surface, which influences the effective mass. This previous work considered the lightest mass direction for resistivity and the average effective mass used for the Seebeck coefficient. The difference in direction leads to decoupling between resistivity and the Seebeck coefficient.[11] The data for $Eu_{11}Zn_{4-x}Cu_xSn_2As_{12}$ show that Cu doping in the defect hexagonal layer does not correlate with the expected 2D material behavior. While the Seebeck values decrease, they remain high and comparable to those of compounds such as $Cu_3Sb_{1-x}Pb_xSe_4$[35] and $Eu_{5-x}A_xSn_2As_6$(A = K).[28]

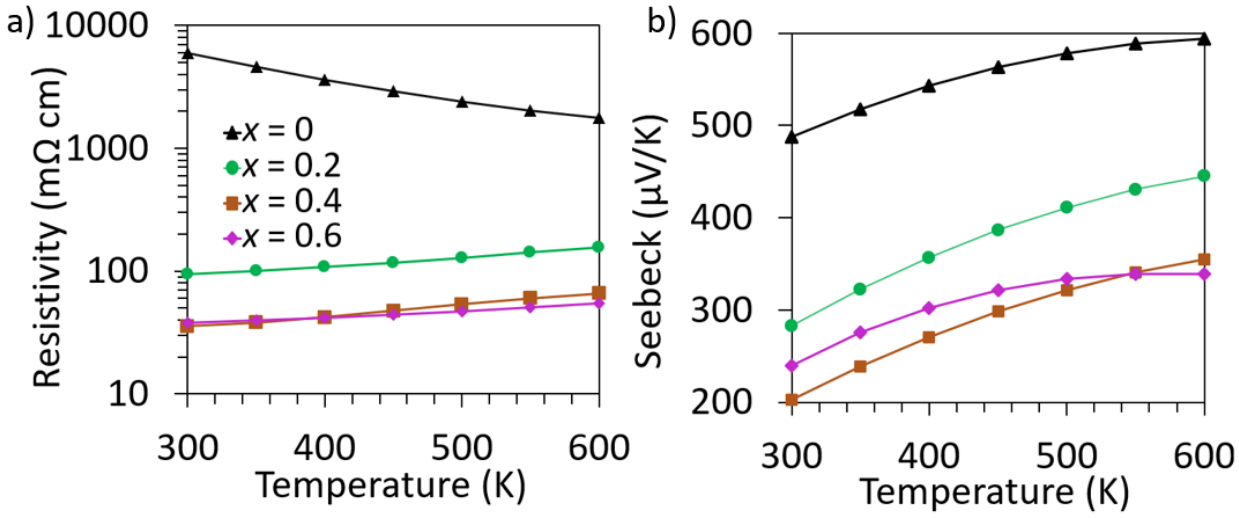


Figure 8. a) Electrical resistivity and b) Seebeck coefficients for $Eu_{11}Zn_{4-x}Cu_xSn_2As_{12}$ (x = 0, 0.2, 0.4, 0.6) from 300 to 600 K.

The temperature-dependent zT for $Eu_{11}Zn_{4-x}Cu_xSn_2As_{12}$ (x = 0, 0.2, 0.4, 0.6) is shown in Figure 9. The maximum zT value is 0.24 at 600 K for $Eu_{11}Zn_{3.4}Cu_{0.6}Sn_2As_{12}$. In the Na-doped $Eu_{11}Zn_4Sn_2As_{12}$, the increase in zT was hypothesized to result from increased carrier density via 2D transport.[11] With the decrease in electrical resistivity obtained for the Cu doped compound, the zT is comparable to that of other hexagonal layered structures.[38] Heating and cooling cycles

for the temperature-dependent Seebeck coefficient for samples x = 0.2 and x = 0.4 are provided in the SI, Figure S10. The values of zT are comparable to compounds such as $EuZn_{0.25}Cu_{0.5}Sb_2$ [39],$CaZn_{0.5}Cu_{0.5}Sb_2$[39] and $Eu_{4.9}La_{0.1}Sn_2As_6$.[28]

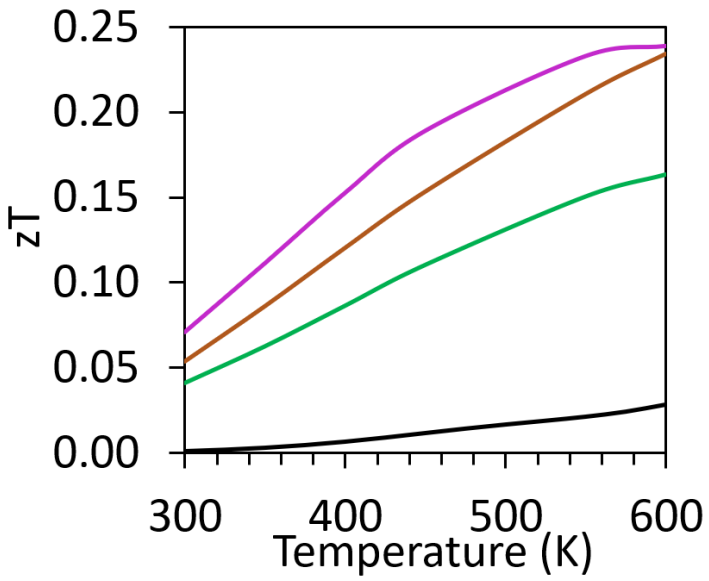


Figure 9. The zT of $Eu_{11}Zn_{4-x}Cu_xSn_2As_{12}$ (x = 0, 0.2, 0.4, 0.6) from 300 to 600 K.

Summary

The thermoelectric properties of Cu doped $Eu_{11}Zn_4Sn_2As_{12}$ were investigated, providing a step forward beyond Na doping of this phase.[11] Powder diffraction and SEM/EDX support the successful incorporation of Cu into the defect hexagonal sheets of $Eu_{11}Zn_4Sn_2As_{12}$. The thermal properties showed that the compound exhibited a low lattice thermal conductivity comparable to $Eu_{21}Zn_4As_{18}$[32] and Eu_2ZnSb_2.[12] Hall data was collected, showing an increase in carrier concentration from 10^{17} to $\sim 10^{19}$ cm^{-3}, and providing strong evidence for Cu doping. Electronic transport properties were measured, and a significant decrease in resistivity is observed compared to the pristine sample (30 mΩ cm). The Seebeck coefficients decrease with increasing Cu content, although they remain high and comparable to those of $Cu_3Sb_{1-x}Pb_xSe_4$.[35] The decoupling of resistivity and the Seebeck coefficient in these 2D materials, as suggested for the Na-doped samples, was not achieved.[11] Since we are no longer in a single parabolic band, as suggested by the weighted mobility plot, the anisotropic Fermi surface implies that the average effective mass used for the Seebeck coefficient differs from the lightest mass used for resistivity. To fully understand the electronic properties, further theoretical calculations will be needed. This combination of variables leads to a $zT_{600K} \sim 0.24$, more than double that of the highest-doped Na sample, which had a $zT \sim 0.09$.[11] By focusing on the unique $[Zn_2As_3]^{5-}$ defect hexagonal layers, we showed that doping on the Zn sites greatly improved their properties.

While doping the $[Zn_2As_3]^{5-}$ layer shows great promise for improving thermoelectric properties with Cu, other dopants may be used to further understand how the layered phase's transport properties change with each one. It would also be useful to study the impact of Cu doping on the magnetic properties of this layered phase. This study shows how tuning a specific layer can yield significant improvements in thermoelectric properties and provides a unique perspective for future studies of other layered Zintl phases.

Author Information

Susan M. Kauzlarich - Department of Chemistry, University of California, Davis, California 95616, United States; Christopher Miramontes Ruiz– Department of Chemistry, University of California, Davis, California 95616, United States; Eric S. Toberer- Department of Physics, Colorado School of Mines, Golden, Colorado 80401, United States; Maria Wróblewska - Department of Physics, Colorado School of Mines, Golden, Colorado 80401, United States

Supporting Information

Plots of Rietveld refinements of the EuAs binary and $Eu_{11}Zn_{4-x}Cu_xSn_2As_{12}$ (x = 0, 0.2, 0.4, 0.6), SEM micrographs and EDS elemental mapping, Table of compositions calculated from SEM/EDS, Weighted mobility plot, plot comparing Cu/Na doped samples versus carrier concentration, and heating/cooling cycles for samples x = 0.2 and x = 0.4.

Acknowledgements

This work was supported by the National Science Foundation, DMR-2307231 and DMR-2350519. The authors are grateful to the UC Davis Center for Nano and Micro Manufacturing (CNM2) and Michelle H. Frasch for collecting EDS/SEM data.

References

(1) Shi, X.-L.; Li, N.-H.; Li, M.; Chen, Z.-G. Toward Efficient Thermoelectric Materials and Devices: Advances, Challenges, and Opportunities. *Chem. Rev.* **2025**, *125* (16), 7525–7724. https://doi.org/10.1021/acs.chemrev.5c00060.

(2) Sun, Q.; Du, C.; Chen, G. Thermoelectric Materials and Applications in Buildings. *Prog. Mater. Sci.* **2025**, *149*, 101402. https://doi.org/10.1016/j.pmatsci.2024.101402.

(3) AL Shurafa, S. M.; Ismail, F. B.; Kazem, H. A.; Almajali, T. A. H.; Ee Sann, T. Experimental Study of Photovoltaic-Thermoelectric Systems Using Thermal Interface Materials and Natural Cooling. *Appl. Therm. Eng.* **2025**, *258*, 124855. https://doi.org/10.1016/j.applthermaleng.2024.124855.

(4) Tang, F.; Chen, Y.; Yu, W.; Chen, Y.; Wang, S.; Zhao, W.; Yin, X.; Liu, Y.; Zhang, X.; Han, Z.; Fang, Y. Anisotropic Magnetic, Magnetotransport, and Electronic Properties of the Layered Zintl Compound $EuAl_2Si_2$. *Phys. Rev. Mater.* **2025**, *9* (6), 064205. https://doi.org/10.1103/llq5-zddh.

(5) Kauzlarich, S. M. Zintl Phases: From Curiosities to Impactful Materials. *Chem. Mater.* **2023**, *35* (18), 7355–7362. https://doi.org/10.1021/acs.chemmater.3c01874.

(6) Baranets, S.; Ovchinnikov, A.; Bobev, S. Structural Diversity of the Zintl Pnictides with Rare-Earth Metals. In *Handbook on the Physics and Chemistry of Rare Earths*; Elsevier, 2021; Vol. 60, pp 227–324. https://doi.org/10.1016/bs.hpcre.2021.07.001.

(7) Mili, I.; Latelli, H.; Ghellab, T.; Charifi, Z.; Baaziz, H.; Soyalp, F. The Study of Structural, Electronic and Thermoelectric Properties of $Ca_{1-x}Yb_xZn_2Sb_2$ (x = 0, 0.25, 0.5, 0.75, 1) Zintl Compounds. *Int. J. Mod. Phys. B* **2021**, *35* (07), 2150100. https://doi.org/10.1142/S0217979221501009.

(8) Jeffrey Snyder, G.; H. Snyder, A. Figure of Merit ZT of a Thermoelectric Device Defined from Materials Properties. *Energy Environ. Sci.* **2017**, *10* (11), 2280–2283. https://doi.org/10.1039/C7EE02007D.

(9) Snyder, G. J.; Toberer, E. S. Complex Thermoelectric Materials. *Nat. Mater.* **2008**, *7* (2), 105–114. https://doi.org/10.1038/nmat2090.

(10) Devlin, K. P.; Kazem, N.; Zaikina, J. V.; Cooley, J. A.; Badger, J. R.; Fettinger, J. C.; Taufour, V.; Kauzlarich, S. M. $Eu_{11}Zn_4Sn_2As_{12}$: A Ferromagnetic Zintl Semiconductor with a Layered Structure Featuring Extended Zn_4As_6 Sheets and Ethane-like Sn_2As_6 Units. *Chem. Mater.* **2018**, *30* (20), 7067–7076. https://doi.org/10.1021/acs.chemmater.8b02749.

(11) Hauble, A. K.; Toriyama, M. Y.; Bartling, S.; Abdel-Mageed, A. M.; Snyder, G. J.; Kauzlarich, S. M. Experiment and Theory in Concert To Unravel the Remarkable Electronic Properties of Na-Doped $Eu_{11}Zn_4Sn_2As_{12}$: A Layered Zintl Phase. *Chem. Mater.* **2023**, *35* (18), 7719–7729. https://doi.org/10.1021/acs.chemmater.3c01509.

(12) Chen, C.; Li, X.; Xue, W.; Bai, F.; Huang, Y.; Yao, H.; Li, S.; Zhang, Z.; Wang, X.; Sui, J.; Liu, X.; Cao, F.; Wang, Y.; Zhang, Q. Manipulating the Intrinsic Vacancies for Enhanced Thermoelectric Performance in Eu_2ZnSb_2 Zintl Phase. *Nano Energy* **2020**, *73*, 104771. https://doi.org/10.1016/j.nanoen.2020.104771.

(13) Wang, C.; Wang, Q.; Zhang, Q.; Chen, C.; Chen, Y. Intrinsic Zn Vacancies-Induced Wavelike Tunneling of Phonons and Ultralow Lattice Thermal Conductivity in Zintl Phase

Sr_2ZnSb_2. *Chem. Mater.* **2022**, *34* (17), 7837–7844. https://doi.org/10.1021/acs.chemmater.2c01430.
(14) Yang, Y.; Cheng, G.; Blawat, J.; Moseley, D. H.; Wang, H.; Devlin, K. P.; Yu, Y.; Hermann, R. P.; Yao, N.; Jin, R.; Xie, W. Crystal Structure and Magnetic Properties in Semiconducting $Eu_{3-\delta}Zn_xSn_yAs_3$ with Eu-Eu Dimers. *J. Appl. Phys.* **2022**, *132* (4), 043902. https://doi.org/10.1063/5.0094013.
(15) Peng, K.; Zhou, Z.; Wang, H.; Wu, H.; Ying, J.; Han, G.; Lu, X.; Wang, G.; Zhou, X.; Chen, X. Exceptional Performance Driven by Planar Honeycomb Structure in a New High Temperature Thermoelectric Material BaAgAs. *Adv. Funct. Mater.* **2021**, *31* (24), 2100583. https://doi.org/10.1002/adfm.202100583.
(16) Dylla, M. T.; Kang, S. D.; Snyder, G. J. Effect of Two-Dimensional Crystal Orbitals on Fermi Surfaces and Electron Transport in Three-Dimensional Perovskite Oxides. *Angew. Chem. Int. Ed.* **2019**, *58* (17), 5503–5512. https://doi.org/10.1002/anie.201812230.
(17) Bilc, D. I.; Hautier, G.; Waroquiers, D.; Rignanese, G.-M.; Ghosez, P. Low-Dimensional Transport and Large Thermoelectric Power Factors in Bulk Semiconductors by Band Engineering of Highly Directional Electronic States. *Phys. Rev. Lett.* **2015**, *114* (13), 136601. https://doi.org/10.1103/PhysRevLett.114.136601.
(18) An, H.; Wang, D.; He, W. Thermoelectric Properties of $AgBiS_2$: Unveiling the Origin of Ultra-Low Lattice Thermal Conductivity and Optimization Strategies for Electrical Performance. *Appl. Phys. Lett.* **2025**, *127* (14), 143903. https://doi.org/10.1063/5.0294211.
(19) Dharmaiah, P.; Heo, M.; Nagarjuna, C.; Jung, S.-J.; Won, S. O.; Lee, K. H.; Kim, S. K.; Kim, J.-S.; Ahn, B.; Kim, H.-S.; Baek, S.-H. Enhancement of Thermoelectric Properties in *p*-Type ZnSb Alloys through Cu-Doping. *J. Alloys Compd.* **2024**, *1004*, 175739. https://doi.org/10.1016/j.jallcom.2024.175739.
(20) Zheng, Z.; Fan, P.; Luo, J.; Liang, G.; Liu, P.; Zhang, D. Enhanced Thermoelectric Properties of Cu Doped ZnSb Based Thin Films. *J. Alloys Compd.* **2016**, *668*, 8–12. https://doi.org/10.1016/j.jallcom.2016.01.207.
(21) Shen, D.; Tai, S. T.; Liu, K.; Wang, W.; Li, H.; Theja, V. C. S.; Chen, C.; Chen, Y. Point Defect Scattering and Phonon Softening for Achieving High Thermoelectric Performance in P-Type ZnSb with Optimal Carrier Concentration. *ACS Appl. Mater. Interfaces* **2025**, *17* (11), 17036–17044. https://doi.org/10.1021/acsami.4c21670.
(22) Devlin, K. P.; Zhang, J.; Fettinger, J. C.; Choi, E. S.; Hauble, A. K.; Taufour, V.; Hermann, R. P.; Kauzlarich, S. M. Deconvoluting the Magnetic Structure of the Commensurately Modulated Quinary Zintl Phase $Eu_{11-x}Sr_xZn_4Sn_2As_{12}$. *Inorg. Chem.* **2021**, *60* (8), 5711–5723. https://doi.org/10.1021/acs.inorgchem.0c03769.
(23) Iandelli, A.; Franceschi, E. On the Crystal Structure of the Compounds CaP, SrP, CaAs, SrAs and EuAs. *J. Common Met.* **1973**, *30* (2), 211–216. https://doi.org/10.1016/0022-5088(73)90107-0.
(24) Perez, C. J.; Qi, X.; Chen, Z.; Bux, S. K.; Chanakain, S.; Li, B.; Liu, K.; Dhall, R.; Bustillo, K. C.; Kauzlarich, S. M. Improved Power Factor and Mechanical Properties of Composites of $Yb_{14}MgSb_{11}$ with Iron. *ACS Appl. Energy Mater.* **2020**, *3* (3), 2147–2159. https://doi.org/10.1021/acsaem.9b02168.

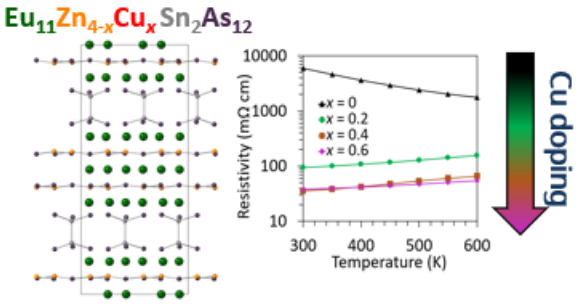
(25) Iwanaga, S.; Toberer, E. S.; LaLonde, A.; Snyder, G. J. A High Temperature Apparatus for Measurement of the Seebeck Coefficient. *Rev. Sci. Instrum.* **2011**, *82* (6), 063905. https://doi.org/10.1063/1.3601358.
(26) Borup, K. A.; Toberer, E. S.; Zoltan, L. D.; Nakatsukasa, G.; Errico, M.; Fleurial, J.-P.; Iversen, B. B.; Snyder, G. J. Measurement of the Electrical Resistivity and Hall Coefficient at High Temperatures. *Rev. Sci. Instrum.* **2012**, *83* (12), 123902. https://doi.org/10.1063/1.4770124.
(27) Yang, X.; Ni, H.; Yu, X.; Cao, B.; Xing, J.; Chen, Q.; Xi, L.; Liu, J.; Zhang, J.; Guo, K.; Zhao, J.-T. Roles of Concentration-Dependent Cu Doping Behaviors on the Thermoelectric Properties of n-Type $Mg_3Sb_{1.5}Bi_{0.5}$. *J. Materiomics* **2024**, *10* (1), 154–162. https://doi.org/10.1016/j.jmat.2023.05.004.
(28) Devlin, K. P.; Gomez, B.; Kauzlarich, S. M. Thermoelectric Properties of P- and n-Type $Eu_5Sn_2As_6$. *Z. Für Anorg. Allg. Chem.* **2022**, *648* (10), e202100386. https://doi.org/10.1002/zaac.202100386.
(29) Kim, H.-S.; Gibbs, Z. M.; Tang, Y.; Wang, H.; Snyder, G. J. Characterization of Lorenz Number with Seebeck Coefficient Measurement. *APL Mater.* **2015**, *3* (4), 041506. https://doi.org/10.1063/1.4908244.
(30) Devlin, K. P.; Grebenkemper, J. H.; Lee, K.; Cerretti, G.; Bux, S. K.; Kauzlarich, S. M. Enhancement of the Thermal Stability and Thermoelectric Properties of $Yb_{14}MnSb_{11}$ by Ce Substitution. *Chem. Mater.* **2020**, *32* (21), 9268–9276. https://doi.org/10.1021/acs.chemmater.0c03043.
(31) Islam, Md. M.; Zheng, J.; Pike, A.; Star, K. E.; Bux, S. K.; Hautier, G.; Kauzlarich, S. M. Diffuson-Driven Lattice Thermal Conductivity in Zintl Arsenides: Disrupting Mass-Thermal Conductivity Relation for High Thermoelectric Performance. *J. Am. Chem. Soc.* **2025**, *147* (46), 42883–42893. https://doi.org/10.1021/jacs.5c15502.
(32) Islam, Md. M.; Wróblewska, M.; Shen, Z.; Toberer, E. S.; Taufour, V.; Kauzlarich, S. M. Magnetism and Thermoelectric Properties of the Zintl Semiconductor: $Eu_{21}Zn_4As_{18}$. *Chem. Mater.* **2024**, *36* (23), 11499–11508. https://doi.org/10.1021/acs.chemmater.4c02200.
(33) Wei, Z.; Li, Z.; Luo, P.; Zhang, J.; Luo, J. Simultaneously Increased Carrier Concentration and Mobility in P-Type $Bi_{0.5}Sb_{1.5}Te_3$ Throng Cd Doping. *J. Alloys Compd.* **2020**, *830*, 154625. https://doi.org/10.1016/j.jallcom.2020.154625.
(34) Chanakian, S.; Peng, W.; Meschke, V.; Ashiquzzaman Shawon, A. K. M.; Adamczyk, J.; Petkov, V.; Toberer, E.; Zevalkink, A. Investigating the Role of Vacancies on the Thermoelectric Properties of EuCuSb-Eu_2ZnSb_2 Alloys. *Angew. Chem. Int. Ed.* **2023**, *62* (29), e202301176. https://doi.org/10.1002/anie.202301176.
(35) Pal, A.; Shyam Prasad, K.; Gurukrishna, K.; Mangavati, S.; Poornesh, P.; Rao, A.; Chung, Y.-C.; Kuo, Y. K. Enhancement of Low-Temperature Thermoelectric Performance via Pb Doping in Cu_3SbSe_4. *J. Phys. Chem. Solids* **2023**, *175*, 111197. https://doi.org/10.1016/j.jpcs.2022.111197.
(36) Raju, C.; Falmbigl, M.; Rogl, P.; Heinrich, P.; Royanian, E.; Bauer, E.; Mallik, R. C. Thermoelectric Properties of Zn Doped Cu_2SnSe_3. *Mater. Chem. Phys.* **2014**, *147* (3), 1022–1028. https://doi.org/10.1016/j.matchemphys.2014.06.054.
(37) Yamashita, A.; Kihou, K.; Kunioka, H.; Nishiate, H.; Yamamoto, A.; Goto, Y.; Mizuguchi, Y.; Iida, T.; Takano, Y.; Lee, C.-H. Thermoelectric Properties of $NaZn_{4-x}Cu_xAs_3$ Crystalized in the

Rhombohedral Structure. *J. Solid State Chem.* **2020**, *291*, 121588. https://doi.org/https://doi.org/10.1016/j.jssc.2020.121588.

(38) Zheng, S.; Peng, K.; Xiao, S.; Zhou, Z.; Lu, X.; Han, G.; Zhang, B.; Wang, G.; Zhou, X. Planar Zintl-Phase High-Temperature Thermoelectric Materials XCuSb (X = Ca, Sr, Ba) with Low Lattice Thermal Conductivity. *J. Adv. Ceram.* **2022**, *11* (10), 1604–1612. https://doi.org/10.1007/s40145-022-0634-y.

(39) Zhang, J.; Liu, X.; Liu, Q.; Xia, S. Structure Transition and Thermoelectric Properties Related to $AZn_{(1-x)/2}Cu_xSb$ (A = Ca, Eu, Sr; 0<x<1) Zintl Phases. *J. Alloys Compd.* **2020**, *816*, 152508. https://doi.org/10.1016/j.jallcom.2019.152508.

TOC


Eu11Zn4-xCuxSn2As12
10000
1000
100
10
Resistivity (mΩ cm)
x = 0
x = 0.2
x = 0.4
x = 0.6
300
400
500
600
Temperature (K)
Cu doping